Particle Physics at CERN

Annual Report 2006

(SNF grants 200020-111728 and 206620-111727)

E. Alagöz, Y. Allkofer, C. Amsler, A. Benelli*, V. Boccone, H. Cabrera, V. Chiochia,
S. Horikawa, C. Hörmann, P. Lightfoot‡, H. Meyer, C. Regenfus, P. Robmann, J. Rochet,
T. Rommerskirchen, T. Speer, S. Steiner, D. Tsirigkas, and L. Wilke.

* visitor from Univ. of Basel
‡ visitor from Univ. of Sheffield

Secretariat: P. Perréard

April 10, 2007

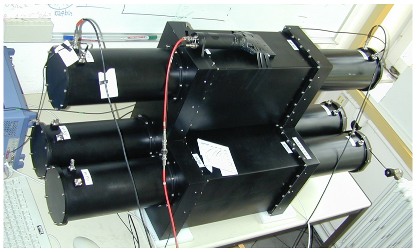

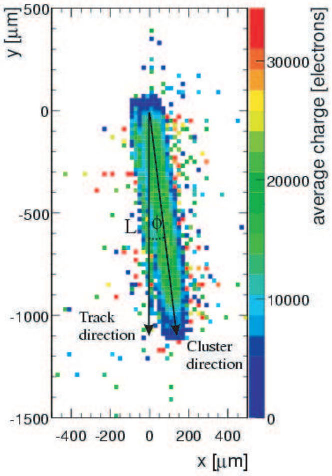

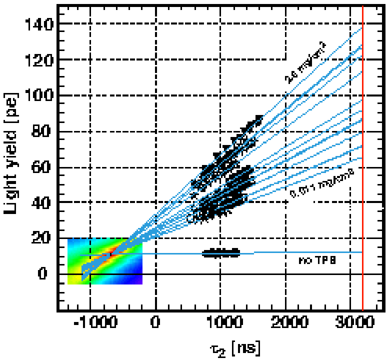

Physik-Institut der Universität Zürich
Winterthurerstrasse 190, CH-8057 Zürich, Switzerland

Contents

1 Particle physics with CMS 3
1.1 Introduction 3
1.2 Reconstruction software 4
1.3 $B_s \rightarrow (J/\psi)\phi$ 4
1.4 $h \rightarrow b\bar{b}$ in SUSY cascades 5
1.5 Pixel sensors and associated software 6
1.6 Pixel efficiency 9
1.7 Detector support structure and service tubes 10

2 Search for $K\pi$-atoms 12
2.1 Introduction 12
2.2 Aerogel Čerenkov-detector 13
2.3 Heavy gas system 16
2.4 Outlook 17

3 Towards a dark matter experiment 18
3.1 Introduction 18
3.2 Photomutiplier operation at low temperature 19
3.3 Light yield in argon 21

4 Publications 24

This report covers the activities of the Zurich group at CERN on the CMS, the DIRAC and the ArDM experiments between 1 April 2006 and 31 March 2007. It does not include the activity of C. Amsler contributing to the "Review of Particle Physics" (Particle Data Group, see J. Phys. G: Nucl. and Part. Phys. **33** (2006) 1). Further details on the group activities and publication reprints can be obtained from our home page (http://www.cern.ch/unizh/).

1 Particle physics with CMS

E. Alagöz, C. Amsler, V. Chiochia, C. Hörmann[1], H. Meyer, C. Regenfus, P. Robmann, J. Rochet, T. Rommerskirchen, T. Speer, S. Steiner, D. Tsirigkas[2], and L. Wilke

In collaboration with:
ETH - Zürich, Paul Scherrer Institut (PSI) and the CMS Collaboration

1.1 Introduction

The main goal of the CMS experiment is to search for the Higgs boson and for physics beyond the Standard Model (SM). The mass of the Higgs can be calculated from the t-quark mass and radiative corrections: M_H <186 GeV (95% CL) [1]. A light Higgs (M_H <130 GeV), decays mainly to $b\bar{b}$, a heavy Higgs mainly to four leptons via W^+W^- or Z^0Z^0. However, for light Higgs the $gg \rightarrow b\bar{b}$ background dominates the $H \rightarrow b\bar{b}$ signal in an inclusive search.

The Minimal Supersymmetric Standard Model (MSSM) is the most popular extension of the SM which stabilizes the Higgs mass and achieves unification at high energies. In addition to SUSY particles the MSSM requires five spin zero fields, the neutral h, H, A and the charged $H^{\pm}$. Two parameters (M_A and tanβ) are needed to fix their masses.

At pp colliders and for small tanβ the h, H, A should be produced dominantly by two gluons through the b- and t-quark loops (fig. 1.1a) supplemented by SUSY contributions. However, large value of tanβ (≥ 5) are favoured [2] in which case the main Higgs production mechanism is radiation off b-quarks (fig. 1.1b).

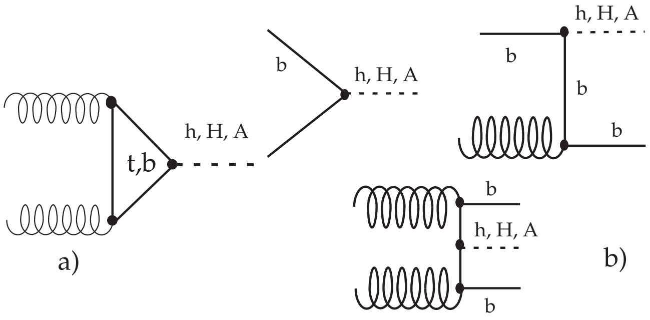

Figure 1.1: *Main contribution to the MSSM Higgs production at the LHC for small tanβ (a). Higgsstrahlung becomes important for large tanβ (b).*

The h lies below 130 GeV and decays dominantly into $b\bar{b}$. The A and H decay into $b\bar{b}$ (or $t\bar{t}$), the H into hh for small tanβ which also lead to b-quarks. Hence the detection of B-mesons is of *crucial importance* in Higgs physics. Several benchmark channels for MSSM Higgs searches have been studied in CMS [3]. The Zurich group is preparing a search for the h associated with the decay of supersymmetric particles. However, during the first two years of LHC operation the luminosity will be well below the design value of 10^{34} cm^{-2}s^{-1} which makes an early discovery of the Higgs unlikely. Meanwhile tools (secondary vertex reconstruction, trigger, b-tagging) need to be developed or tuned with early data. We therefore plan to examine first b-physics issues, hence decays of B-mesons.

Many properties of the B_s, such as the differences between the masses and widths of the two weak eigenstates (B_S^H and B_S^L), can be studied with the decay $B_s \rightarrow (J/\psi)\phi$. A full reconstruction of the B_s can be achieved through the decays $J/\psi \rightarrow \mu^+\mu^-$ and $\phi \rightarrow K^+K^-$. First measurements of the mass difference Δm_s between B_S^H and B_S^L have recently been reported from the Tevatron [4].

---

[1] Until June 2006

[2] CERN doctoral student

However, the difference between their widths, $\Delta\Gamma_s$, has not been measured with sufficient precision to be compared with the SM prediction ($\Delta\Gamma_s/\Gamma_s \sim 0.1$).

The $B_s \rightarrow (J/\psi)\phi$ decay also provides one of the best ways to determine the height of the unitarity triangle. One would measure the (CP-violating) asymmetry between $B_s \rightarrow (J/\psi)\phi$ and $\bar{B}_s \rightarrow (J/\psi)\phi$ which requires tagging the flavor of the B_s. An alternative method is to measure the angular distributions of the final state K's and μ's which are different for the CP-even and CP-odd components. This does not require tagging but large data samples which can be obtained at the LHC.

The Zurich group is contributing to the CMS experiment since 1995. We are involved in the reconstruction software, in particular track and vertex reconstruction [5, 6] and constraining kinematic fits [7]. We are preparing the analysis of $B_s \rightarrow (J/\psi)\phi$ and a search for the MSSM Higgs bosons decaying into, or associated to, $\bar{b}b$ pairs. We are contributing to the innermost device, the barrel pixel detector, with which secondary vertices from B-decays can be determined. We have measured on CERN test beams the performance of pixel sensors before and after irradiation. Many details can be found in ref. [8]. We have contributed to the development of the readout chip and of the power distribution system. We are constructing the mechanical support structure for the pixel detector and the service tubes which provide the coolant and power, and transfer the signals to and from the pixel detector.

1.2 Reconstruction software

In 2006 we ported the track and vertex algorithms (previously written in ORCA) to the new reconstruction environment (CMSSW) while maintaining the performance demonstrated in the Physics TDR [9]. For the vertex reconstruction we had to rewrite the software and adapt the various fitters (Kalman, Gaussian-sum , and kinematic fits, see previous annual reports).

The CMS b-tagging working group, led by one of us (T.S.), is responsible for the development of b-tagging, offline vertex reconstruction algorithms and high level trigger (HLT) for b-decays. The main feature used to distinguish b-jets from light flavour jets is the long lifetime of B-hadrons. The simplest algorithm (used in the HLT) is based on the large impact parameter with respect to the primary vertex. More elaborate algorithms identify the b-decay vertex and select large decay lengths to reject the short-lived background. Further properties can be used, such as the large mass of the b-quark and the high (> 4) final state multiplicity.

The detection of an electron (or a muon) can be used, the semileptonic branching fraction of b-quarks to an electron being of the order of 10%. We are contributing to the reconstruction of electrons from semileptonic b-decays. Some b-jets contain electrons with follow curved trajectories in the magnetic field until they reach the electromagnetic calorimeter. Without tracker material the projection of the trajectories in the transverse plane would be circular, leading to energy deposits in the calorimeter extending over a small number of crystals. However, bremsstrahlung photons from the tracker material leads to azimuthal smearing of the energy deposits. We have improved on algorithms to disentangle energy deposits from different electrons and have included them in CMSSW.

1.3 $B_s \rightarrow (J/\psi)\phi$

This channel has been chosen a a benchmark channel by the CMS collaboration [3]. In the offline analysis the decay $B_s \rightarrow (J/\psi)\phi \rightarrow \mu^+\mu^-K^+K^-$ is reconstructed by combining a pair of $\mu^+\mu^-$ tracks with two additional tracks of opposite charges. As CMS does not possess a particle identification system all tracks have to be considered as possible kaon candidates. A kinematic fit is applied in which the four tracks are constrained to a common vertex and the $\mu^+\mu^-$ invariant mass is constrained to the mass of the J/ψ.

A maximum likelihood fit of the decay angular distribution was performed on a sample of 14'000 simulated events, together with background events such as the dominant $B \rightarrow J/\psi X$. The decay $B_d \rightarrow J/\psi\, K^{*0} \rightarrow \mu^+\mu^-K^+\pi^-$ is of particular concern, since the pion can be confused with a kaon. This final state also displays a time-dependent angular distribution similar to that of B_s-decay. The modelling of the reconstruction efficiency for the decay length is delicate. Without appropriate correction the events at large decay lengths lead to shorter lifetime measurements (fig. 1.2, left).

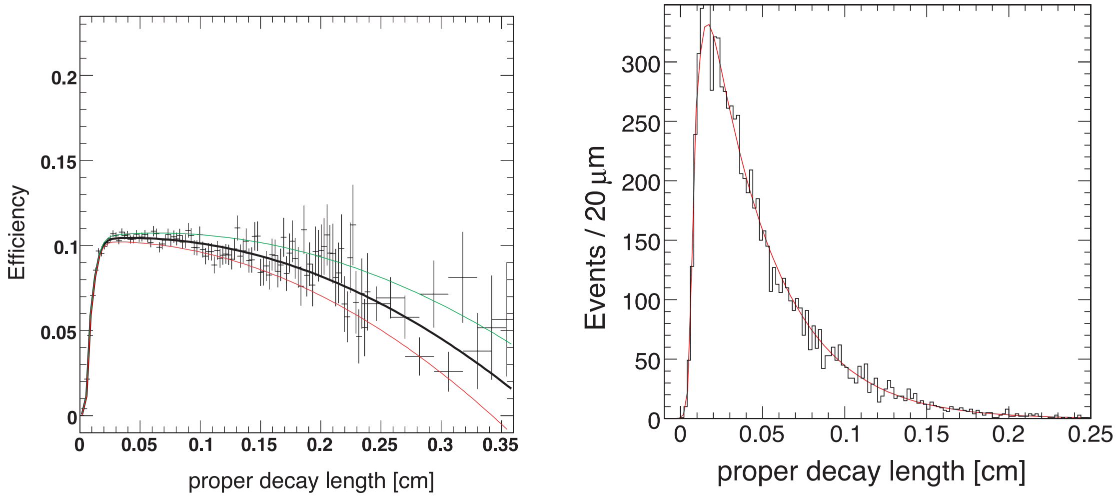

Figure 1.2: *Left: distribution of the B_s-detection efficiency as a function of proper decay length with fit function and 1σ uncertainties. Right: B_s-decay length distribution with fit in red.*

The analysis of $B_s \rightarrow (J/\psi)\phi$ assumes a HLT trigger to enrich the B_s-sample. (We are also developing a trigger for other b-channels such as $B_d \rightarrow J/\psi K^* \rightarrow \mu^+\mu^-K^+\pi^-$ or $B_s \rightarrow \mu^+\mu^-$). In a first step one searches for two muons in the CMS muon chambers with transverse momenta above 3 GeV/c. In the HLT b-candidates are identified through partial reconstruction of the decay products in restricted tracking regions. The muon tracks are then precisely reconstructed and the b-decay vertex determined. A minimum distance from the primary vertex is required and J/ψ events are selected by a cut on the 2μ-invariant mass. The efficiency of the trigger for $B_s \rightarrow (J/\psi)\phi \rightarrow \mu^+\mu^-K^+K^-$ events is 20%.

The resolution on the B_s-invariant mass after kinematic fit is 14 MeV and the resolution on the proper decay time 77 fs [7]. The decay length distribution is shown in fig. 1.2, right. The results show that we will be able to measure a value of say $\Delta\Gamma_s/\Gamma_s = 0.20$ with an uncertainty of 20%. To investigate the influence of $\Delta\Gamma_s$ on the measurement a simple Monte-Carlo simulation was developed which produces events according to the angular (time-dependent) distribution smeared with the experimental resolution. From these studies we conclude that the statistical error on $\Delta\Gamma_s/\Gamma_s$ will decrease to 5% for 110'000 events (corresponding to 10 fb^{-1}) at which point the systematic error will start to dominate.

1.4 $h \rightarrow b\bar{b}$ in SUSY cascades

The lightest Higgs (h) can be produced in cascades between SUSY particle, e.g. $\tilde{\chi}^0_2 \rightarrow \tilde{\chi}^0_1 h$, $h \rightarrow b\bar{b}$, where $\tilde{\chi}^0_1$ is the lightest neutralino (possibly the WIMP of dark matter searches). These cascades start with the production of squarks and gluinos and can be identified through their comparatively large number of high energetic jets. In R-parity conserving supersymmetry the $\tilde{\chi}^0_1$ (with mass around 200 GeV) is stable. Since dark matter has survived until today, $\tilde{\chi}^0_1$ must be interacting only weakly with matter. Its signature in the CMS detector would therefore be a large missing energy. This signature offers a possibility to tag events for which the main decay mode $h \rightarrow b\bar{b}$ is otherwise hard to distinguish against QCD background. Previous studies showed that a 5σ discovery should be possible with 2 fb^{-1}[10] and thus a signal could be observed rather early at LHC. Efficient b-tagging algorithms are crucial to distinguish the b-jets in Higgs decay from those in other processes. Figure 1.3 shows an example of b-tagging efficiency based on PYTHIA and the CMSSW reconstruction software: as expected, efficient b-tagging also leads to a high background from lighter quarks.

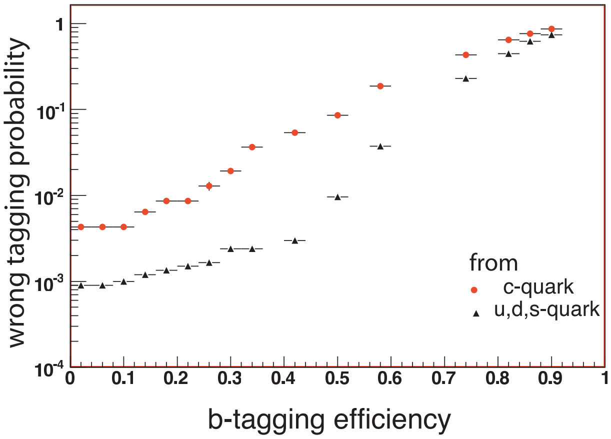

Figure 1.3: *b-tagging efficiency vs. wrong tagging probability from c- or u-, d-, or s-jets.*

1.5 Pixel sensors and associated software

The pixel barrel detector consists of three concentric cylindrical layers, 53 cm long, with radii of 4.4, 7.3 and 10.2 cm. The pixel sensors are made of n^+-structures on n-bulk silicon. They are mounted on segmented silicon plates connected by indium bump bonds to the readout chips. The analogue signals are read out to determine the coordinates more accurately, using charge sharing between pixels.

We have tested sensor prototypes with 105 – 225 GeV pions in the H2 beam line of the CERN SPS. Earlier results can be found e.g. in ref. [11] or in previous annual reports. In particular, we have demonstrated that the charge collection profiles measured in our beam tests and the expected trapping rates can be described by a two trap model producing a non-constant space charge density across the sensor bulk [12]. This leads to electric field profiles with two maxima across the sensor bulk, one at each sensor edge. The model is supported by measurements of the electric field profile based on its dependence on the electron mobility. The measurements were obtained with a novel method using our test beam data [13]. From these tests sensors with moderate p-spray isolation where chosen and the pixel size was fixed to 100×150 μm^2.

Our 2006 results on the position resolution are based on simulations relying on test beam data which were collected with pixels of dimensions 125×125 μm^2. The spatial resolution is improved after irradiation by applying so-called η-corrections to the charges collected on adjacent pixels (for details see our previous annual report). Figure 1.4 shows a simulation of the residual distribution (measured – predicted) for clusters of two pixels and tracks with an angle $\alpha = 20°$ with respect to the normal to the sensor surface. The sensor is assumed to have been irradiated with 5.9×10^{14} $\text{n}_\text{eq}/\text{cm}^2$, which corresponds to the first four years of LHC operation for the innermost layer. The distribution before correction is not described by a single Gaussian and is affected by large systematic errors which depend on the interpixel hit position. The width can be largely reduced by applying η-corrections (inset in fig. 1.4). A position resolution below 15 μm can be achieved for perpendicular tracks in the CMS transverse plane [14], even after heavy irradiation. Table 1.1 summarizes the expected spatial

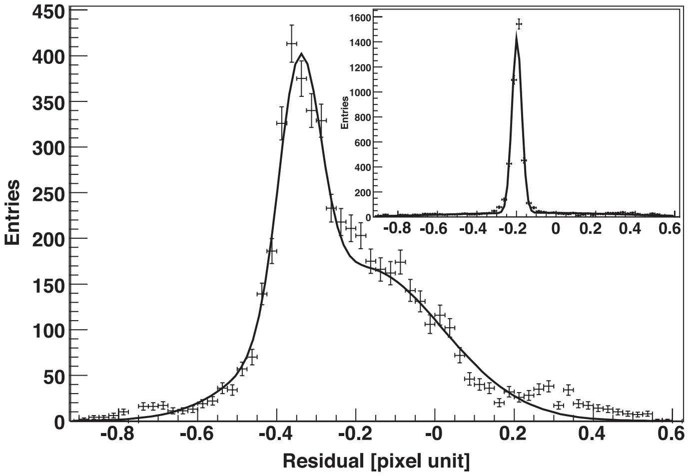

Figure 1.4: *Distribution of residuals for incident tracks with* $\alpha = 20^\circ$ *and sensors irradiated to* 5.9×10^{14} $n_{\rm eq}$*/cm*^{2}*. The continuous line is a double-Gaussian fit to the distribution. The inset shows the results with* η*-corrections. The residuals are not corrected for the Lorentz shift due to the magnetic field (from ref. [14]).*

Φ ($n_{\rm eq}$/cm^2)	V$_{bias}$ [V]	Resolution [μm]
0	200	9.0±0.1
2×10^{14}	200	12.1±0.2
6×10^{14}	300	12.9±0.1

Table 1.1: *Expected position resolution for perpendicular tracks at various irradiation fluences* Φ *and bias voltages* V_{bias}*.*

resolution for perpendicular tracks and different irradiation fluences.

Another beam test was performed at CERN in 2006 with the final pixel sizes (100 × 150 μm^2) and its front-end electronics in a 3T magnetic field. Data were taken with irradiated and unirradiated pixel sensors with different chip calibration settings and bias voltages. The goal of this test was to study the position resolution of barrel pixel sensors before and after irradiation, with and without magnetic field, and to compare with expectations (table 1.1).

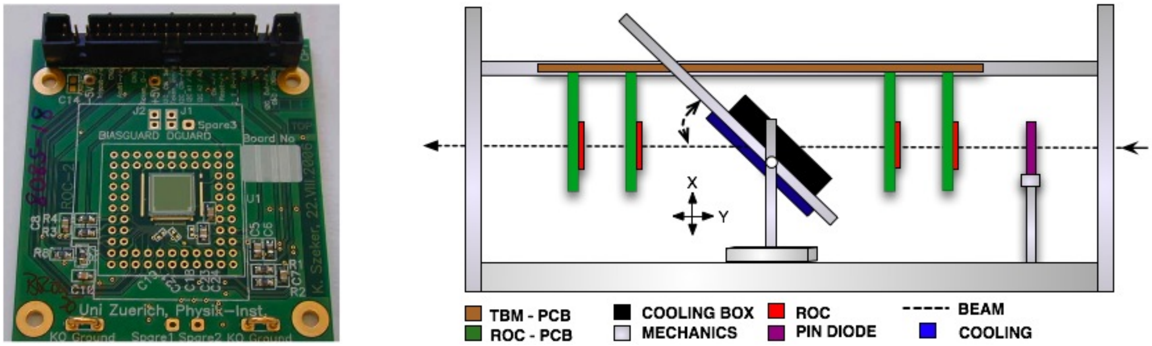

Figure 1.5: *Left: PCB housing a pixel sensor bump-bonded to the ROC. Right: Setup used for our recent pixel test (see text).*

The experimental setup (fig. 1.5, right) consisted of a pixel sensor bump-bonded to a readout chip (ROC), a cooling device, a trigger system, a precise telescope to measure the direction of the incident pions, and a data acquisition system. The setup was located in a 3T Helmholtz coil with magnetic field perpendicular to the beam. The sensors (52 × 80 pixels) were bump-bonded to the ROC at PSI and irradiated at the CERN IRRAD1 facility with 24 GeV protons. The irradiation fluences varied from

0.37×10^{14} to $8.2 \times 10^{14} \mathrm{n_{eq}cm^{-2}}$. The irradiated samples were wire-bonded to a printed circuit board designed in our electronics workshop in Zurich (fig. 1.5, left).

The beam telescope was made of four pixel sensor planes, bump-bonded to ROCs. Two of the planes were placed in front and two behind the test sensor. The beam telescope was used to determine accurately the hit position and incident angle on the test sensor. The planes were tilted by 20° to enhance charge sharing (and hence position resolution). The tested sensor was located in a cool box equipped with two cooling Peltier elements for operation at $-10°\mathrm{C}$. The hot sides of the Peltier elements were cooled with water and nitrogen gas was flushed in the cooling box to avoid condensation. The cooling box could be rotated for measurements at different incident angles. A trigger signal was provided by a 2×6 mm^2 PID diode which was synchronized to the SPS beam clock (40 MHz).

The analysis of this data is in progress. Preliminary results indicate that the measured charge distribution and cluster mutiplicity agree with expectations.

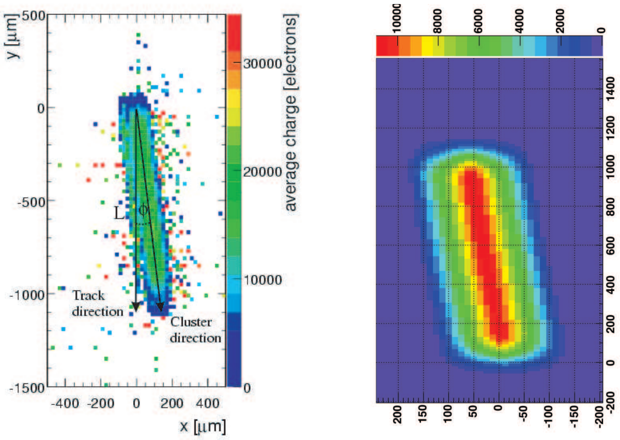

Figure 1.6: *Left: average charge of clusters produced by 10 GeV muons in the first pixel barrel layer for $\eta \sim 2$, as a function of distance from the track entry point (simulation). The y-coordinate is parallel to the beam direction. The collected charge is shifted along the x-coordinate due to the Lorentz effect. Right: real data from a beam test at 3T.*

In 2006 we also used our two-trap model to develop new reconstruction algorithms and calibration procedures for irradiated pixel sensors. The drifting electrons experience the Lorentz force in the 4T field of CMS and drift perpendicularly to the magnetic and biasing electric field. Figure 1.6 (left) shows the average charge collected in a pixel cluster as a function of distance from the track entry point. The figure is produced assuming 10 GeV muons at a pseudorapidity $\eta \sim 2$ and using the full CMS detector simulation. The Lorentz angle Θ_L can be extracted from this figure using the relation $\tan \Theta_L = \frac{L}{T} \tan \phi$ where L is the cluster length along the track direction and $T = 285$ μm is the sensor thickness. Figure 1.6 (right) shows the effect from test beam data for comparison.

Due to radiation damage the sensor response is expected to change during detector operation and several quantities have to be monitored to guarantee a precise determination of the hit positions. One of us (V.C.) is leading the pixel Data Quality Monitoring group (DQM). Data monitoring will be performed online and offline and includes raw hits, reconstruction of hit clusters and multiplicities, pixel track seeds, distribution of primary vertices from pixel tracks and impact parameters.

In particular, the Lorentz deflection leads to a shift of the hit coordinate (fig. 1.4) which needs to be corrected. The correction (which can reach 120 μm) will change as a function of time and as a function of location due to radiation damages which modify the electric field distribution. The Lorentz angle will therefore be monitored in-situ. We wrote the software to extract the Lorentz deflection angle directly from CMS data. Since the three barrel layers will be exposed to different fluences, the Lorentz angle must be measured in each detector layer as a function of pseudorapidity. The shift can be determined for a given ionization depth in the sensor using a large number of well measured tracks (fig. 1.7, left). The detector is subdivided into its three cylindrical layers with eight rings for various

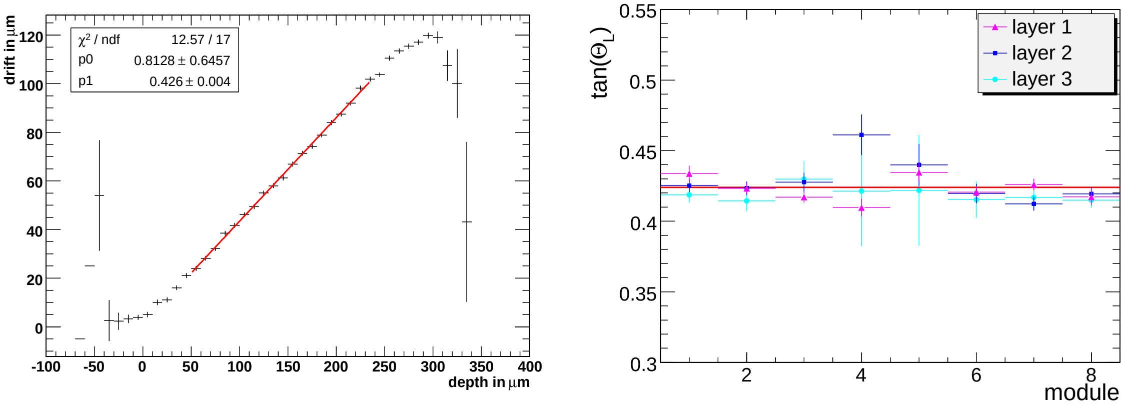

Figure 1.7: *Left: shift of the hit coordinate due to the Lorentz drift as a function of depth at which the charge is produced in the sensor (simulation of non-irradiated sensors). The value for tan* Θ_L *is read from the slope of the fit (in red). Right: reconstructed Lorentz angle angle for the 24 rings. The horizontal red line is the value assumed for the simulation.*

pseudorapidities. A separate fit is performed for each of the 24 rings. The reconstructed Lorentz angle from simulated $Z^0 \to \mu^+\mu^-$ events agrees with the assumed value in the simulation (fig. 1.7, right).

We are currently developing applications for visualizing DQM histograms (web interface) and generate alarms. The DQM software will be tested with the pixel detector hardware during the integration phase planned for the first half of 2007.

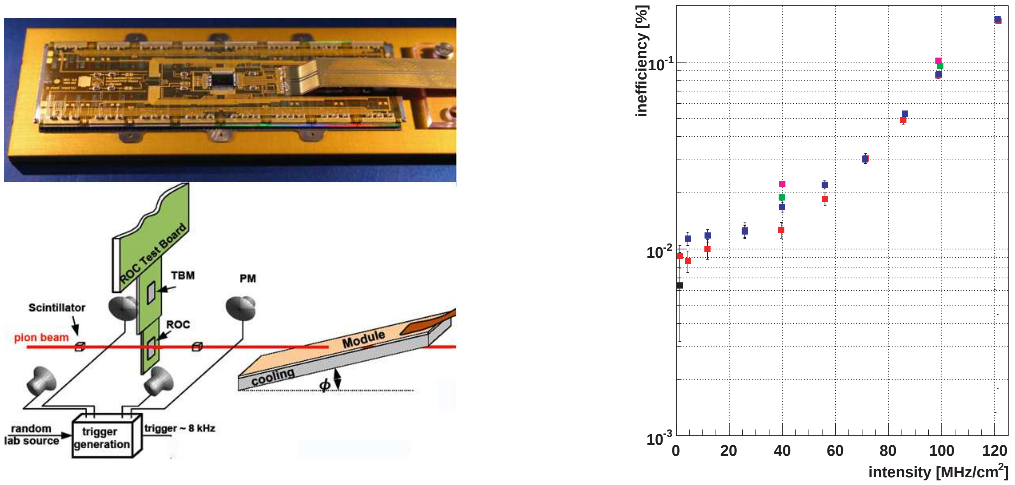

Figure 1.8: *Pixel readout module (top left) and beam setup to measure the inefficiency shown on the right for different trigger rates (for details see ref. [15]). The flux at the innermost pixel layer in the LHC will be 60 MHz/cm*^{2}.

1.6 Pixel efficiency

The performance of the barrel modules was studied in a recent PhD thesis [15]. A module is made of 16 ROCs connected to the 66’560 pixels by the bump bonding technique. We measured the inefficiency under LHC conditions in a high rate pion beam at PSI and compared with simulations. The setup is shown in fig. 1.8 (left). The inefficiency is about 2% for the innermost layer (fig. 1.8, right). Let us mention in particular the problem of Single Event Upsets (SEUs) which are due to the harsh radiation environment, causing corrupted memory cells. This was studied and alleviated with protection capacitors yielding about 1 SEU/s for the entire pixel barrel detector ($\sim 48 \times 10^6$ pixels) at full luminosity [15]. This development is now completed and mass production is underway at PSI.

1.7 Detector support structure and service tubes

The support structure for the barrel pixel detector and the corresponding service tubes are currently under construction in the Institute's workshop. The 5m long assembly is made of two separated half shells containing the detector and two service half shells at each end (fig. 1.9). The detector endflanges were finalized in 2006 and adapted to the detector endring prints. The flanges consist of thin fibreglass frames (FR4) filled with foam (Airex) covered by carbon fibre blades. The endflanges support the individual detector ladders of the three layers. The endring prints connect the detector modules mounted on the ladders to the readout electronics installed in the corresponding readout slots of the service tubes.

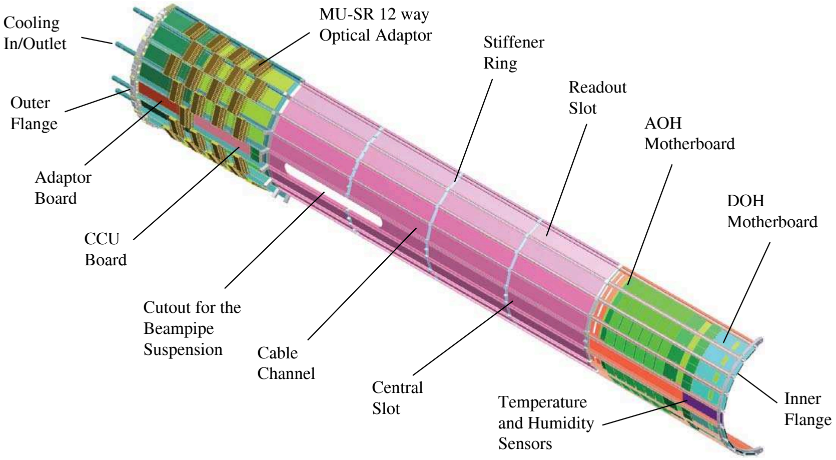

Figure 1.9: *Overview of a supply tube half shell.*

The various components, such as carbon fibre blades and cooling containers, were produced in 2006 and the assembly of the support structure has started. The power, the cooling fluid, the control and the optical signals are transferred through the service tubes to the pixel detector (fig. 1.9). The massive cables are attached to the outer flange. The structure is supported by stainless steel tubes (wall thickness of 100 μm) connected to the stiffener rings and the inner and outer aluminium flanges. The tubes also supply the detector with the cooling fluid. The gaps are filled with Airex foam.

We have also designed the printed circuit supply boards (motherboards and readout electronics). The motherboards which hold the optical hybrids for the analogue and digital control links are installed in eight readout slots near the detector on the integrated supply boards. The corresponding boards at the outer ends carry the power adaptor boards, which provide the detector power and the bias voltage. In the central slot the digital communication and control board (CCU) is installed which distributes the control signals to the individual readout boards of the eight readout sectors and collects the information on temperature, pressure and humidity. The optical fibres are loosely installed in the cable channels.

Our electronics workshop is involved in the pixel detector front end control system. It consists of four CCUs, each controlling a quarter of the detector (eight barrel sectors). Figure 1.10 shows the block diagram of a CCU Board.

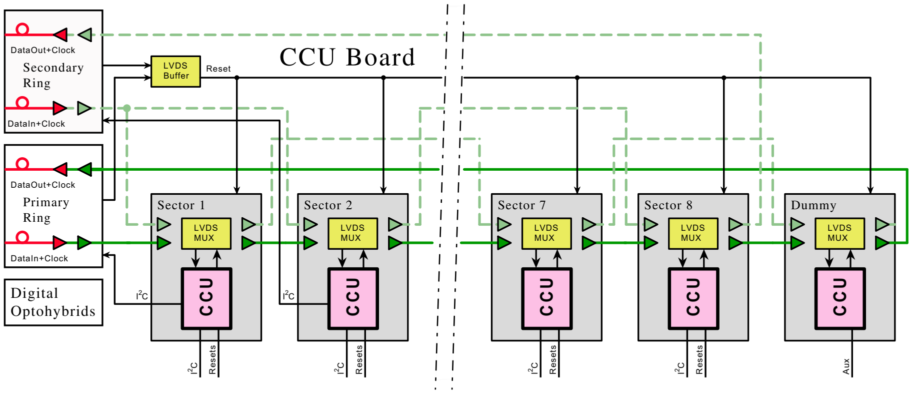

Figure 1.10: *Block diagram of the Barrel Pixel control system. Only 5 of the 9 CCUs are shown for simplicity. One CCU board controls eight readout sectors of the barrel pixel detector.*

Our group is also responsible for the design of the CMS pixel detector power distribution for the front end electronics (low voltage) and the pixel sensors (high voltage), and cabling. The power lines are integrated in the service tubes. The high and low DC voltages are generated with a commercial modular system manufactured by CAEN. The system has to cope with sudden (100 ns) current excursions of 2 A in 50 m long power lines.

The detector support structure for the three layers will be ready in August 2007 and the pixel detector will be installed in CMS in January 2008.

References

[1] LEP Electroweak working group (2005), http://lepewwg.web.cern.ch/LEPEWWG/

[2] For a brief summary, see C. Amsler, “SM and MSSM Higgs at the LHC”, http://amsler.web.cern.ch/amsler/Higgs.pdf

[3] The CMS collaboration, “CMS Physics Technical Design Report Volume II: Physics Performance”, CERN/LHCC 2006-021, CMS TDR 8.2, 2006

[4] V.M. Abazov *et al.*, Phys. Rev. Lett. **97** (2006) 021802;
A. Abulencia *et al.*, Phys. Rev. Lett. **97** (2006) 062003

[5] R. Frühwirth and T. Speer, Nucl. Instr. and Meth. in Phys. Res. **A 534** (2004) 217

[6] R. Frühwirth, K. Prokofiev, T. Speer, P. Vanlaer and W. Waltenberger, Nucl. Instr. Meth. in Phys. Res. **A 502** (2003) 699

[7] K. Prokofiev, PhD Thesis, Universität Zürich (2005)

[8] Y. Allkofer *et al.*, submitted to Nucl. Instr. Meth. in Phys. Res. **A**, prep. physics/0702092 (2007)

[9] The CMS collaboration, “CMS Physics Technical Design Report Volume I: Detector Performance and Software”, CERN/LHCC 2006-001, CMS TDR 8.1, 2006

[10] F. Moortgat, P. Olbrechts, L. Pape and A. Romeyer, CMS Note 2006/090

[11] A. Dorokhov *et al.*, Nucl. Instr. Meth. in Phys. Res. **A 530** (2004) 71

[12] V. Chiochia *et al.*, IEEE Trans. Nucl. Sci. **52** (2005) 1067;
V. Chiochia *et al.*, Nucl. Instr. Meth. in Phys. Res. **A 568** (2006) 51;
M. Swartz *et al.*, Nucl. Instr. Meth. in Phys. Res. **A 565** (2006) 212

[13] A. Dorokhov *et al.*, Nucl. Instr. Meth. in Phys. Res. **A 560** (2006) 112

[14] E. Alagoz, V. Chiochia, M. Swartz, Nucl. Instr. Meth. in Phys. Res. **A 566** (2006) 149

[15] C. Hörmann, PhD Thesis, Universität Zürich (2006)

2 Search for $K\pi$-atoms

Y. Allkofer, C. Amsler, A. Benelli[3], S. Horikawa, C. Regenfus, and J. Rochet

In collaboration with:
Basel, Bern, Bucarest, CERN, Dubna, Frascati, IHEP-Protvino, KEK, Kyoto, Moscow, Prague, Santiago, Tokyo and Trieste

(DIRAC-II Collaboration)

2.1 Introduction

The $K^+\pi^-$-atom is a hydrogen-like non-relativistic system of a K^+ and a π^- bound by the Coulomb force. The binding energy of the 1s level is 2.9 keV. The atomic level is broadened and shifted by the overlap of the pion and kaon nuclear wave functions. The atom is unstable and decays into $K^0\pi^0$. Such atoms have not been observed so far, but $\pi^+\pi^-$ atoms were studied by the DIRAC Collaboration at CERN [1]. The lifetime of the 1s level is related to the difference $|a_1 - a_3|$ between the $K\pi$ S-wave scattering lengths a_1 and a_3 corresponding to the isospin 1/2 and 3/2 states, respectively.

A measurement of the scattering lengths is important for chiral perturbation theories (ChPT). In contrast to $\pi^+\pi^-$-atoms, the $K\pi$-scattering length probes ChPT extended to s-quarks in the limit where the masses of the u-, d- and s-quarks vanish. The scattering lengths can be obtained by extrapolation to zero energy from the isospin 1/2 and 3/2 S-wave phase shifts, however with substantial uncertainties due to the lack of good low energy $K\pi$-scattering data. The extrapolations from the various scattering measurements disagree by large factors: measurements of a_1 vary between 0.17 and 0.34 m_π^{-1}, those of a_3 between –0.07 and –0.14 m_π^{-1}. The scattering lengths were also computed from dispersion relations using scattering data, assuming analytical continuation, unitarity and crossing symmetry [2]:

$$a_1 = 0.224 \pm 0.022\ \mathrm{m}_\pi^{-1}\ \text{ and }\ a_3 = -0.0448 \pm 0.0077\ \mathrm{m}_\pi^{-1}. \tag{2.1}$$

However, there are inconsistencies below 1 GeV/c [2]. Assuming the above values one predicts a mean life $\tau \sim$ 3.7 fs for the $K\pi$-atom. Note that a 20% measurement error in the lifetime leads to a 10% error in $|a_1 - a_3|$. Details on the physics motivations can be found in our 2005 annual report.

In DIRAC-II [3] our group provides the aerogel Čerenkov counters and the heavy gas system for kaon detection. Kaons and pions are produced by the 24 GeV/c PS proton beam on target, typically a 100 μm thick nickel foil [4]. The emerging particles are analyzed in a double-arm magnetic spectrometer measuring the momentum vectors of two oppositely charged hadrons (fig. 2.11). The dissociated kaon and pion from $K\pi$-atoms emerge behind the target with a very small relative momentum $Q <$ 3 MeV/c. $K^+\pi^-$-atoms, once produced, move forward and annihilate into $K^0\pi^0$, are being excited or ionize in the target. Since annihilation, excitation and ionization are competing processes, one can determine the mean life by measuring the (calculable) breakup probability in the target.

Detecting Čerenkov radiation from kaons in the DIRAC-II momentum range between 4 and 8 GeV/c requires a transparent medium with a refractive index of typically $n = 1.015$. This can be achieved with aerogel. However, the suppression of fast protons at small angles with respect to the primary beam line requires an even smaller refractive index of typically 1.008. Unfortunately the light yield decreases rapidly with refractive index, and hence R&D developments were required to achieve a reasonable light collection efficiency.

---

[3] Visitor from the University of Basel

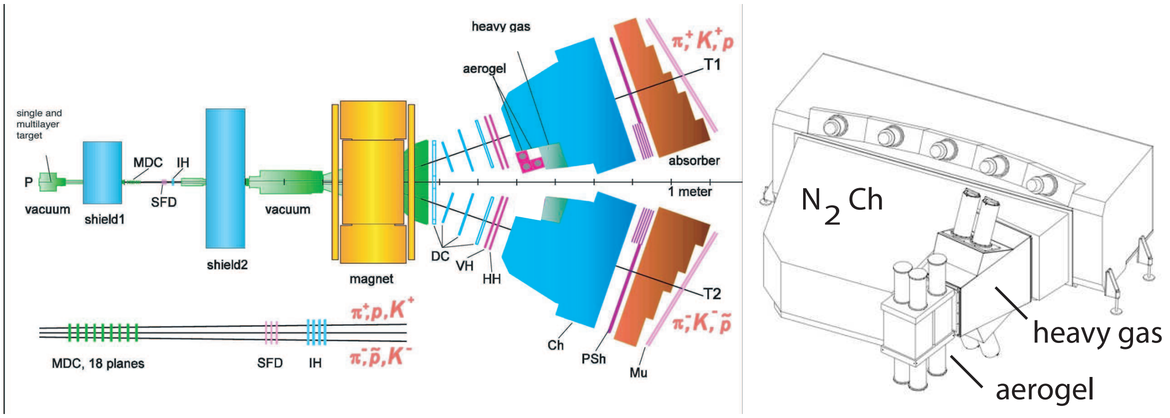

Figure 2.11: *Sketch of the updated DIRAC-II spectrometer showing the locations of the Čerenkov counters to identify electrons, pions and kaons. MDC = microdrift chambers, SFD = scintillator fibre detector, IH = ionization hodoscope, DC = drift chambers, VH, HH = scintillation hodoscopes, Ch =* N_2*-Čerenkov counter, PSh = preshower, Mu = muon counters. Right: aerogel, heavy gas and* N_2*-Čerenkov counters.*

On the other hand, the faster pions and the beam contaminating electrons will also be detected by our aerogel counters. The latter are vetoed by an N_2-Cerenkov counter and the former by a heavy gas Čerenkov detector (see fig. 2.11) for which we developed the gas distribution system. Positive kaons are detected in the left arm with the aerogel counter which also suppresses the overwhelming background from scattered protons. On the other hand, the background from antiprotons in the right arm is small so that negative kaons from $K^-\pi^+$-atoms do not need to be detected directly with an aerogel counter.

2.2 Aerogel Čerenkov-detector

In 2006 the design of the aerogel Čerenkov-counter for kaon-proton separation was finalized, the detector constructed and installed in the DIRAC-II experiment. The final detector consists of three independent modules (fig. 2.12). Two of them have aerogel with the refractive index $n = 1.015$ for kaon-proton separation between 4 and 5.5 GeV/c (24ℓ supplied by Panasonic) and the third one has the lower index $n = 1.008$ for 5.5 to 8 GeV/c kaons (13ℓ purchased from the BINP/BIC Institutes in Novosibirsk).

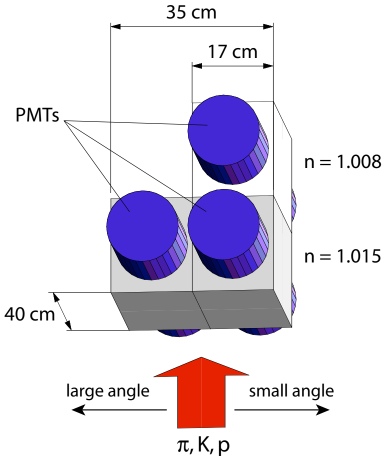

Figure 2.12: *Sketch of the three aerogel counters, each read out by two (5") Photonis XP4570B photomultipliers (PMT) with UV window. Fast protons populate the small angle region with respect to the primary beam axis and are vetoed with the* $n = 1.008$ *aerogel module.*

The light yield is proportional to the factor $1-1/\beta^2 n^2$ (where β is the kaon velocity) and therefore becomes very small for low refractive indices. On the other hand, the Čerenkov light intensity is inversely proportional to the wavelength and hence concentrated in the UV-region. We have determined the light yield for kaons using a test setup, cosmic rays and simulation (fig. 2.13).

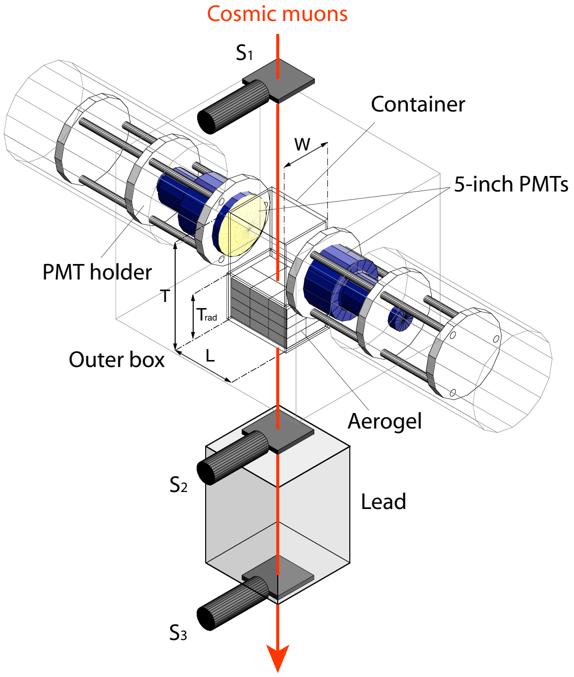

Figure 2.13: *Apparatus used to measure the light yield of aerogel and the detection efficiency of Čerenkov light with cosmic rays. High energy muons are selected with the lead absorber between the scintillation counters S_2 and S_3.*

The light detection efficiency for kaons traversing the aerogel at equal distance (20 cm) from the two PMTs is reduced by roughly 50% compared to kaons passing near one of the photocathodes. For a 17 cm thick aerogel detector with refractive index $n = 1.008$ we expect between 4 and 7 photoelectrons from kaons at 7 GeV/c, depending on the impact position. However, the light absorption length depends strongly on wavelength and increases rapidly from about 10 cm at 270 nm to 3 m at 350 nm. The loss due to absorption can be compensated by using a wavelength shifter and also by increasing the radiator thickness at the center of the detector.

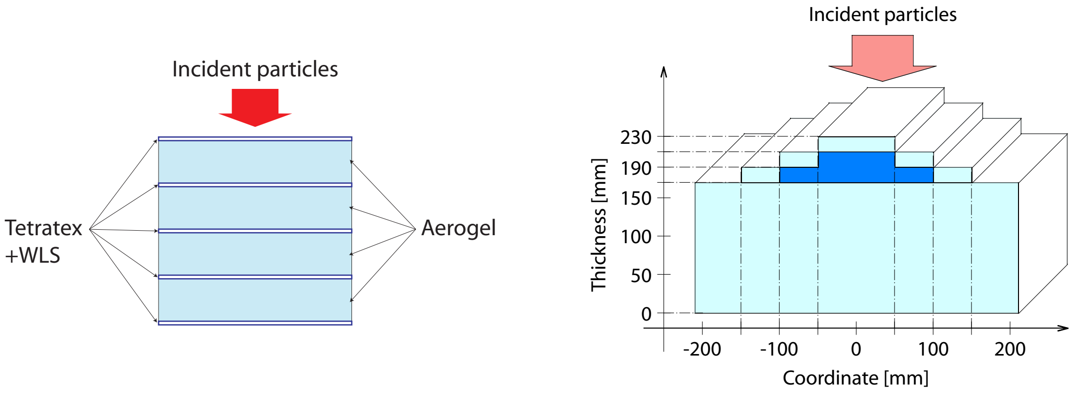

Figure 2.14: *Principle of the aerogel sandwich counter (left) and pyramidal structure (right).*

To compensate for the low Čerenkov light yield in the 1.008 counter and to increase the absorption length we have developed a novel sandwich design consisting of aerogel tiles interleaved with a wavelength shifter (WLS) coated reflector (such as Tetratex), as illustrated in fig. 2.14 (left). The goal was to shift the Čerenkov UV towards blue light, thereby increasing the absorption length by two orders of magnitude, and also matching the photocathode sensitivity of the PMT. The best results were obtained with Tetratex as reflector immersed in a solution of p-terphenyl dissolved in chloroform for the WLS. This technique increased the light detection efficiency by 50%. Details on these developments can be found in our 2005 annual report and in a recent publication [5].

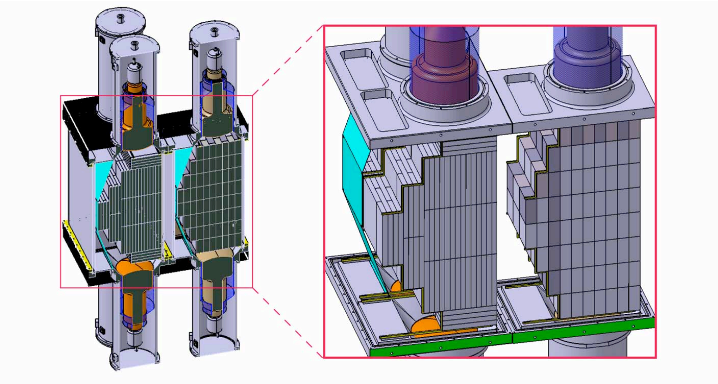

Figure 2.15: *Drawing of the final setup. The aerogel tiles are arranged in a pyramidal geometry in a steel box that also supports the housing of the PMTs and their mu-metal shields. The steel box is shielding the PMTs from the fringe field of the DIRAC dipole magnet.*

On the other hand, the pyramidal shape compensates for the stronger absorption in the center (fig. 2.14, right). The thickness of the 1.008 aerogel radiator varies from 16 to 23 cm, the thickness of the 1.015 radiator from 11 to 23 cm. A drawing of the final detector is presented in fig. 2.15. The inner container surfaces are covered with three layers of Tetratex. The aerogel tiles are held by a steel frame covered with TiO_2 paint as diffuse reflector. The 1.008 pyramid contains 236 and the 1.015 pyramids 124 extremely fragile aerogel tiles which are held with a coarse mesh made of 250 μm thick threads.

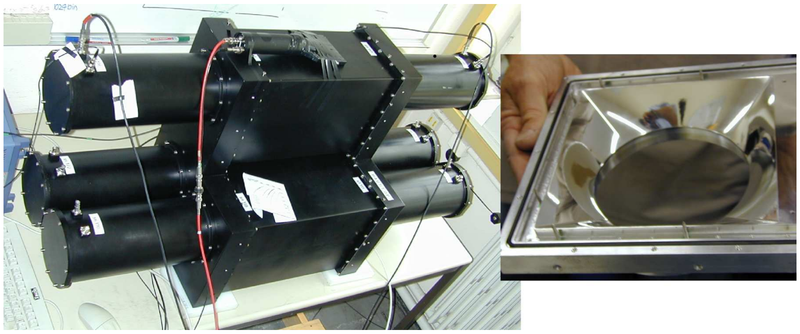

Figure 2.16: *Left: completed left arm detector. Right: spherical mirrors to focus the light on the PMT photocathodes.*

Figure 2.16 shows the completed apparatus in our laboratory, ready for tests with cosmic ray muons, since test beams were unfortunately not available at CERN in 2005 and early 2006. The aluminium coated spherical mirrors are covered with an MgF_2 layer for which the thickness was optimized to the emission spectrum of the WLS. Apart from the mirrors most of the mechanical structure was built in the Institute's workshop. The cosmic ray test showed that the light yield did not depend significantly on the impact position (fig. 2.17). For the 1.015 detector we obtained about 6.4 photoelectrons for cosmic muons, implying ~ 5 photoelectrons for 4 GeV/c kaons. The performance of the 1.008 counter could not be tested with cosmic rays.

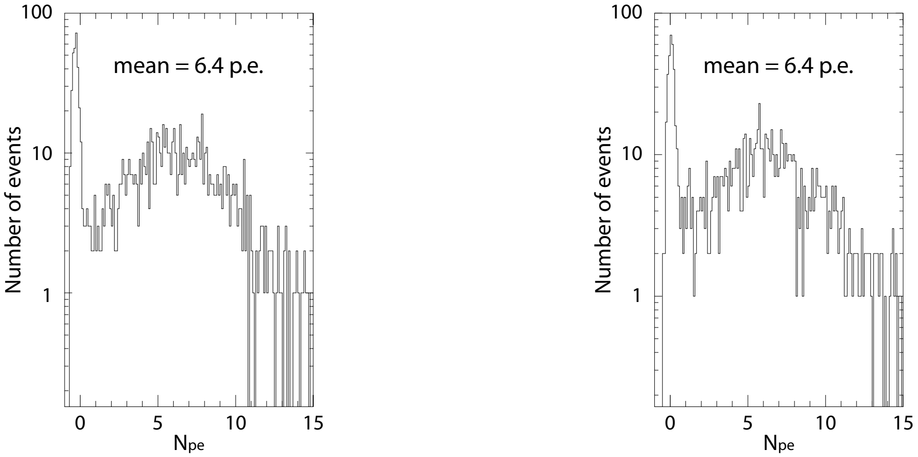

Figure 2.17: *Amplitude distribution (number of photoelectrons) for the 1.015 modules from cosmic muons passing near the PMT (left) and in the middle of the counter (right).*

2.3 Heavy gas system

The Zurich group has also designed and built a gas recirculation system for the heavy gas Čerenkov counter. We are using C_4F_{10} (perfluorobutane) with a refractive index of 1.00137 (at 300 nm and 1 bar) to detect pions in the range 4 – 9 GeV/c, while suppressing kaons. The system (fig. 2.18) is inspired from RICH counters used in other experiments (such as COMPASS). We purchased 30 kg of C_4F_{10} liquid from F2 Chemicals [6] Ltd., enough for four years of measurements, taking into account the unavoidable losses.

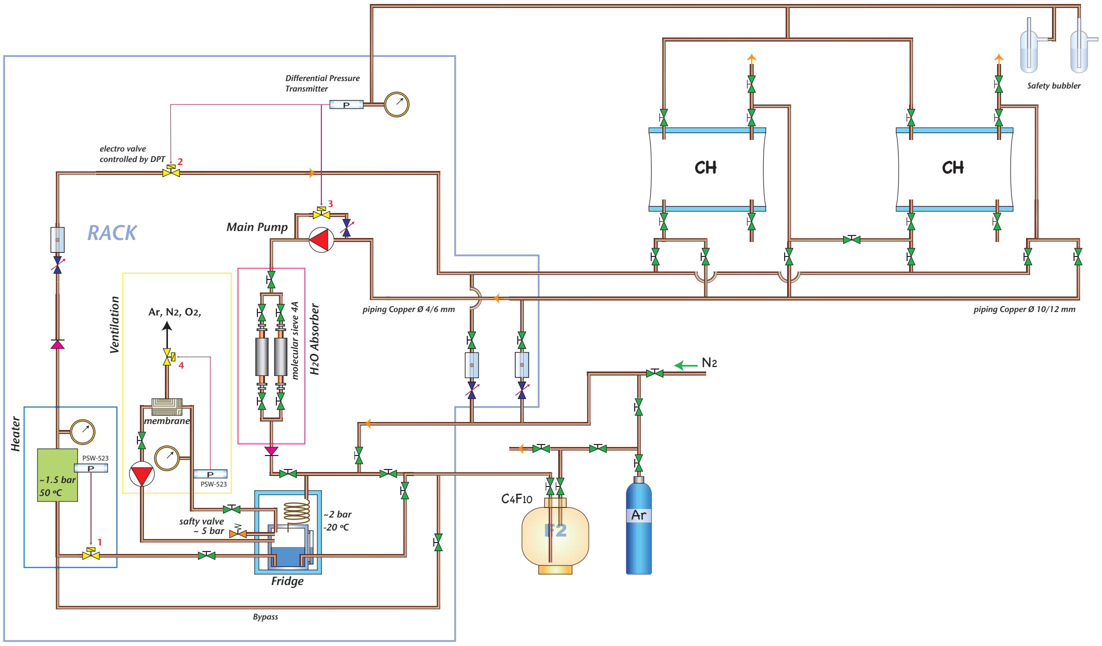

Figure 2.18: *C_4F_{10} gas recirculation system. Important functions such as gas purification, pressure regulation and main circulation pump are integrated in the gas rack on the left. Valves near the two detector vessels (left and right arms of DIRAC-II) allow various circulation and recovering modes.*

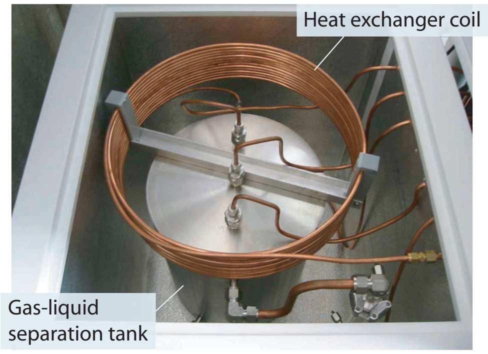

Figure 2.19: *Inside the freezer: the C_4F_{10} gas returning from the detector flows through a heat exchanger coil and is liquefied before being restored in the gas-liquid separation tank.*

C_4F_{10} liquid is first transferred from the gas bottle to the gas-liquid separation tank in the freezer (-18°C) shown in fig. 2.19. The inner pressure is raised to $\sim$2 bar by the main pump to liquefy the gas, while contaminants such as nitrogen, oxygen or argon remain gaseous. This gas mixture is circulated through a hollow-fiber membrane module [7] transparent to smaller molecules. These contaminants are thus vented to the air. The purified liquid is then transferred to the gas buffer which is heated up to 50°C. The gas returning from the detector flows through molecular sieves (4 Å) which absorb water vapor. The pressures in the separation tank and in the gas buffer are regulated using small mechanical pressure switches and electrovalves to ensure a constant flow. The tank, the buffer and the molecular sieve cylinders were constructed in our Institute's workshop.

2.4 Outlook

The aerogel detector was installed in the DIRAC-II beam line in summer 2006. The beam was turned on in late August but was soon interrupted by repeated failures of a switching magnet in the CERN primary proton beam line. This unfortunately led to the cancellation of data taking in 2006. A replacement magnet will be provided for the 2007 runs. The C_4F_{10}-Čerenkov counter was built and installed with the help of our Russian collaborators in October 2006 and the assembly of the gas system was completed the following month.

Meanwhile we are developing the analysis programs. The software is being tested with data taken in 2001 to determine the lifetime of $\pi^+\pi^-$-atoms. So far some 12'000 $\pi^+\pi^-$-atoms have been observed by DIRAC. We plan to use only the detectors downstream of the dipole magnet (see fig. 2.11). This would increase the available data sample by about a factor of 2 – 3, but presumably also increase systematic errors.

The yield of $K\pi$- atoms is expected to be about 25 $\times$ lower than for $\pi^+\pi^-$-atoms. Assuming equal acceptances and the increase in beam flux by a factor of two, this should lead to about 1'000 reconstructed $K^+\pi^-$- (and $K^-\pi^+$-) atoms during three months of data taking.

References

[1] B. Adeva *et al.* (DIRAC Collaboration), Phys. Lett. **B 619** (2005) 50
[2] P. Büttiker, S. Descotes-Genon, B. Moussallam, Eur. Phys. J. **C 33** (2004) 409
[3] B. Adeva *et al.*, Addendum to DIRAC proposal, CERN - SPSC - 2004 - 009
[4] B. Adeva *et al.*, Nucl. Instr. and Meth. in Phys. Res. **A 515** (2003) 467
[5] Y. Allkofer *et al.*, submitted to Nucl. Instr. and Meth. in Phys. Res. **A**
[6] F2 Chemicals Ltd., http://www.fluoros.co.uk/
[7] O. Ullaland, Nucl. Instr. and Meth. in Phys. Res. **A 553** (2005) 107;
we thank Olav Ullaland from CERN for his advice in developing the heavy gas system.

3 Towards a dark matter experiment

C. Amsler, V. Boccone, H. Cabrera, S. Horikawa, P. Lightfoot[4], C. Regenfus, and J. Rochet

In collaboration with:
CIEMAT, ETHZ, Soltan Institute (Warsaw), Universities of Granada and Sheffield

(ArDM Collaboration)

3.1 Introduction

In 2006 we continued the development of the light readout system for the ArDM dark matter experiment. We plan to use a one ton liquid argon time projection chamber to detect recoil nuclei from the scattering of Weak Interacting Massive Particles. WIMPs are among the favorite candidates for the missing non-baryonic matter in the universe, and the prominent candidate is the lightest supersymmetric (SUSY) particle, the neutralino, with a mass of at least 40 GeV. The experimental upper limit for the cross-section of WIMPs with nucleons is about 10^{-6} pb, a cross section that would lead to 100 events per day in the ArDM detector, assuming a detection threshold of 30 keV for recoil argon nuclei.

Details on the experiment can be found in our previous annual report and in ref. [1]. The drifting electron charge from ionizing recoils and the VUV scintillation light (128 nm) will be recorded with high efficiency to suppress the electron background from the radioactive β-emitter ^{39}Ar. Its activity in natural ^{40}Ar argon has been measured to be about 1 Bq/kg [2], therefore inducing a background rate of about 1 kHz in a one ton detector. The rejection of the γ- and β-background will be achieved through the combined measurement of the charge-to-light ratio, the time structure of the light signal, and the determination of the interaction point on an event-by-event basis.

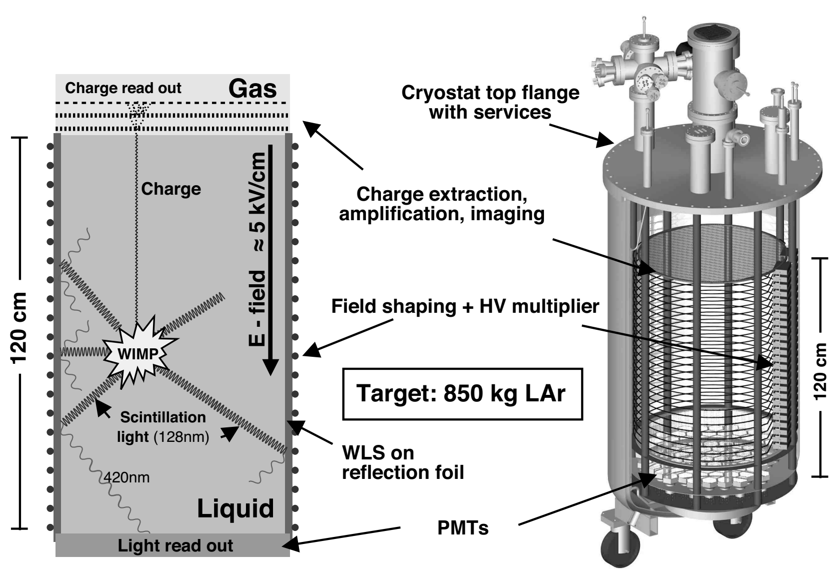

Figure 3.20: *Detection principle and 3D-drawing of the ArDM detector.*

The ratio of primary scintillation light to ionization charge collected after a given drifttime in an external electric field is different for nuclear recoils and minimum ionizing particles, being very high for the former, due to quenching. This provides the main discrimination between WIMPs and

---

[4] Visitor from the University of Sheffield

background. On the other hand, the VUV photons are produced from the spin singlet and triplet states of the excited dimer A_2^*, following ionization, which have different lifetimes (τ = 7 ns, resp. 1.6 μs in liquid [3]). These states are populated differently according to the excitation process: for heavy ionization (such as nuclear recoils) the singlet dominates, while for minimum ionizing particles (such as electrons) the triplet dominates [3]. Hence the discrimination of decay time allows a further separation between WIMP induced recoils and background from γ or electrons.

The working principle of the two-phase detector is shown in fig. 3.20 (left). A WIMP interaction leading to 30 keV recoils produces about 400 VUV photons, together with a few free electrons. The strong vertical electric field (5 kV/cm) sweeps the electrons to the top surface of the liquid and extracts them into the gas phase. After multiplication ($\approx 10^5$) in a two stage Large Electron Multiplier (LEM) the charges are collected by a segmented anode. The VUV light is emitted isotropically from the interaction point and converted to blue light by a wavelength shifter (WLS) on the side walls. The shifted and reflected light is collected at the bottom of the cryostat by 14 phototubes (8") immersed in the liquid. The 3D-CAD sketch (fig. 3.20, right) shows the mechanical design of the prototype detector and the cryostat. Not shown is the (non-conductive) wavelength shifting foil inside the field shapers.

3.2 Photomutiplier operation at low temperature

Low temperature photomultipliers (PMTs) covering a surface of $\approx$1.5 m^2 and immersed in liquid argon will be used in the ArDM experiment. A bialkali photocathode has a quantum efficiency of typically 30% at room temperature, but becomes insulant at liquid argon temperatures ($\approx$ 88K). A platinum (Pt) underlay under the photocathode is necessary to restore the electron population in the photocathode. Unfortunately, this solution also reduces the quantum efficiency to $\approx$15%.

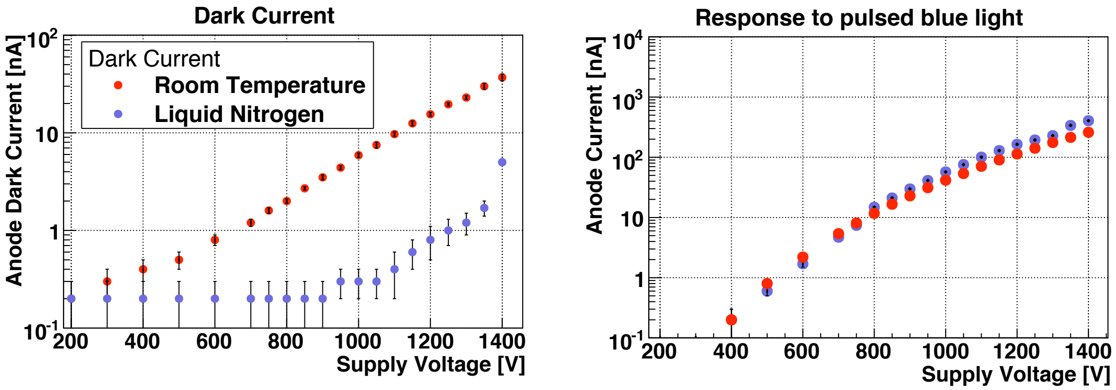

Figure 3.21: *Dark current (left) and response to blue light of the Hamamatsu PMT vs. bias for room and liquid N_2 temperature.*

We have investigated two 3" PMTs for their functionality and quantum efficiency at low temperature. The best result was obtained with a square 8-dynode tube from Hamamatsu (R6237-MOD) manufactured with Pt-underlay. The dark current (thermal emission rate × gain) and the response to light (gain) were measured. Figure 3.21 shows the expected decrease of dark current for the Hamamatsu tube at low temperature, while the light response remains constant (the slight increase in fig. 3.21 is attributed to a gain fluctuation).

To optimize the light collection efficiency we performed various measurements with different setups, reflectors material and WLS. For example, the glass window of PMTs can be coated with

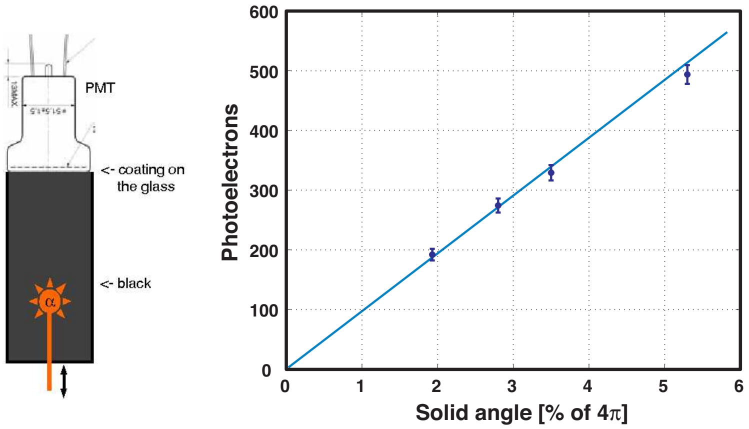

Figure 3.22: *Left: experimental setup. Right: number of photoelectrons from the 5.3 MeV α-source as a function of the solid angle subtented by the Hamamatsu R6237-MOD PMT in argon gas.*

a WLS within a matrix of paraloid or polystyrene [4], giving thin transparent wavelength shifting layers. Light emitted from the WLS in the (optically dense) matrix is trapped and efficiently produces photoelectrons at the photocathode. Efficient conversion of VUV light was observed by coating the PMT glass surface with tetraphenylbutadiene (TPB) dissolved in paraloid or polystyrene (PS). The layer (1 μm thickness) was deposited by dissolving TPB/PS in chloroform and dipping the PMT in the solution. A black box filled with argon gas and a 5.3 MeV moveable α- source were used (fig. 3.22, left). The number of photoelectrons was measured for different distances between the PMT and the α-source. As expected, the data expressed as a function of solid angle is compatible with a straight line. We obtained 480 photoelectrons for a 5% solid angle, which corresponds to a quantum efficiency of about 12%.

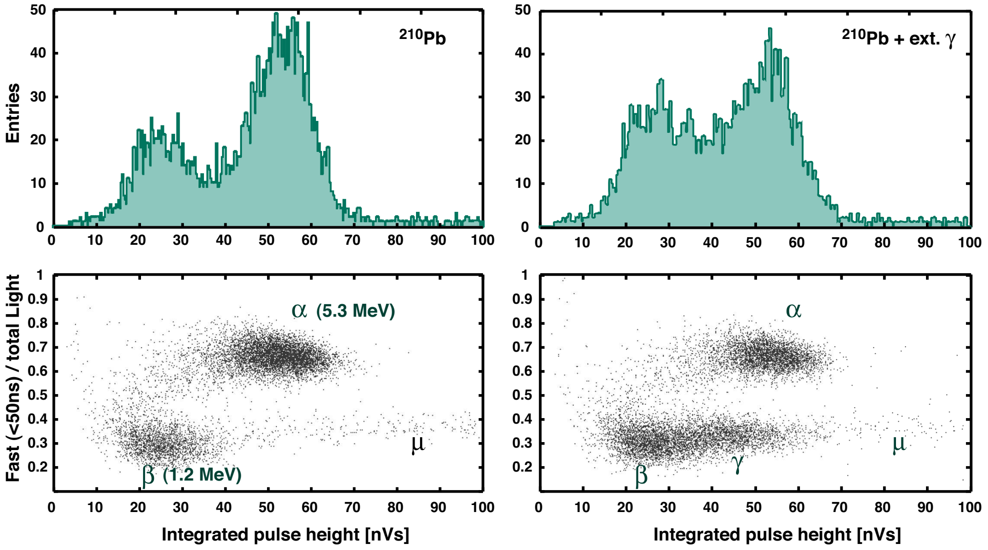

Figure 3.23: *Ratio R of fast to total light output vs. time integrated amplitude with (left) and without (right) external γ source.*

3.3 Light yield in argon

We have determined the light yield in gaseous and liquid argon and established the ratio of singlet to triplet contributions. Our measurements in gas with a 5ℓ vacuum chamber showed that the number of photoelectrons depends crucially on the purity of argon, the contribution from the slow component and its decay time increasing with purity (see our previous annual report). The two decay components were clearly observed with a mean life of 15.7 ± 4.0 ns for the fast (singlet) and 3.12 ± 0.08 μs for the slow (triplet) component [5]. The latter is in good agreement with literature, 3.2 ± 0.3 μs [6]. A first attempt to measure the singlet to triplet population ratio in liquid is shown in fig. 3.23. The plots show the ratio R of fast ($<$ 50 ns) to total light output vs. total amplitude for the Po α-source (left) and with an additional external γ-source (right). One observes a clear separation between heavily ionizing projectiles and electrons.

Figure 3.24 shows the improved apparatus built in 2006. Two Hamamatsu (R6237-MOD) PMTs face one another. The cell volume is roughly 1ℓ and an α-source is located in the center. The PMT glass surfaces are coated with a transparent TPB/paraloid layer. The side walls consist of 10 × 10 cm^2 foils with evaporated TPB. The analogue signal from the PMT is sampled by a 1 GHz digital oscilloscope, stored to hard disk and analysed offline. A baseline correction is performed with the portion of the signal before trigger time. The noise is determined by the amplifier. The number of detected photons is calculated as usual by dividing the integrated charge by the average single photon charge, which we find from distributions of dark counts and LED light pulses.

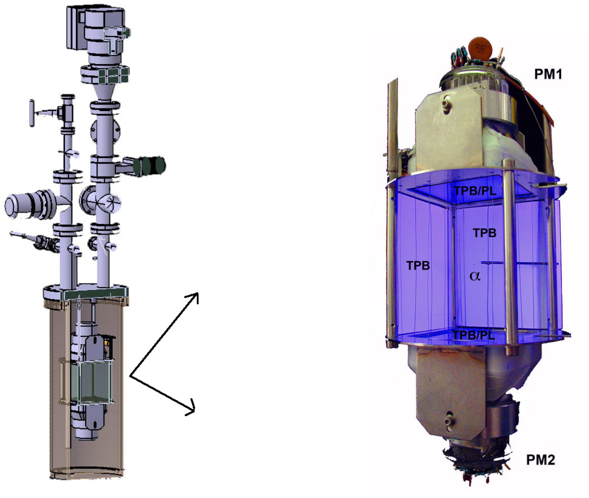

Figure 3.24: *Left: 2006 setup. Right: enhanced view of the liquid argon cell cell under UV illumination.*

From several measurements with the old and the new setup we find an average value for the triplet to singlet ratio of 6.0 ± 1.8 for 5.3 MeV α in argon gas at NTP. The error was estimated from fluctuations among the data sets. The largest measured value for the triplet decay time τ_2 = 3.12 μs, mentioned above, was found for the purest argon gas. Impurities in argon gas were found to reduce the scintillation light by shortening the decay time τ_2. This effect was studied in detail by mixing argon gas with air at partial pressures between 1 and 10^{-6} mbar [5]. For the various partial air pressures the averaged α-signals were fitted and analysed, as described above. Figure 3.25 (left) shows the yields obtained for the fast and slow components vs. τ_2. The contribution from the slow component increases linearly with τ_2, reaching to 3.2 μs in gas at NTP, while the fast component remains constant. This behaviour can be explained as due to the non-radiative destruction of the triplet excimer states by gas impurities. This is presumably due to residual water, since cooling improves on the light yield (and τ_2).

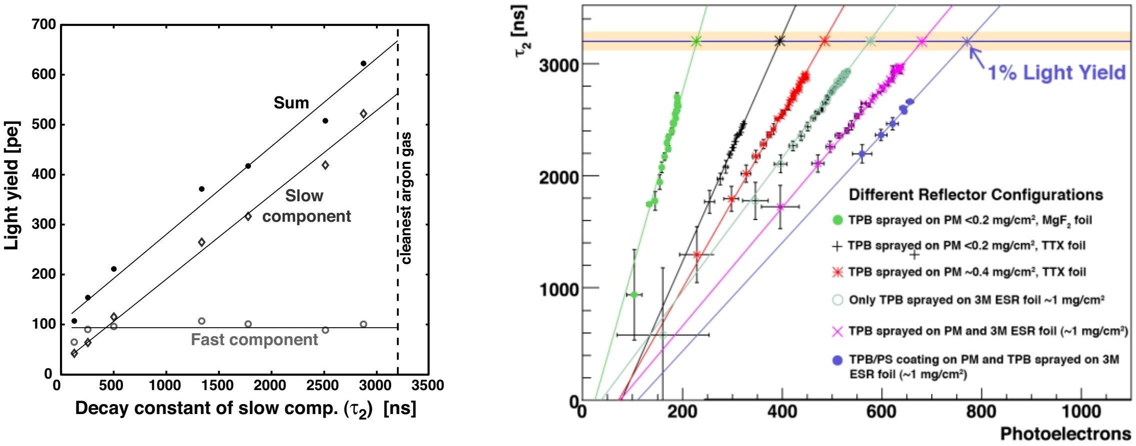

Figure 3.25: *Left: light yield (number of photelectrons) in gaseous argon (NTP) as a function of τ_2. The measurements correspond to different partial air pressures. Right: τ_2 vs. number of photoelectrons for various coatings and reflectors.*

Figure 3.25 (right) shows measurements done with different coatings and reflectors. From the known yield of VUV photons (78 k / α-particle [7]), we find the detection efficiencies (defined as the ratio of detected photoelectrons to emitted UV photons) for the different designs by extrapolating to τ_2 = 3.2 μs. The best result (1% detection efficiency) was achieved with TPB evaporated on 3M reflective foils.

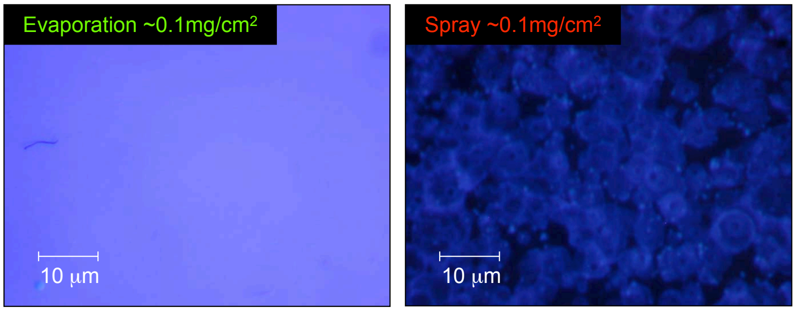

Figure 3.26: *Microscope comparison between evaporated and sprayed TPB, illuminated by UV light.*

Evaporation leads to a much more uniform coating than spraying (fig. 3.26). We have determined the optimum thickness of TPB wavelength shifter to be evaporated on the 3M reflector by using the black box setup shown in fig. 3.22 above. A small glass exsicator was modified to include a heated crucible. The layer thickness of TPB was calculated by weighing the foil before and after vacuum evaporation. Figure 3.27 (left) shows the expected linear correlation beween the deposited thickness and the mass of TPB prepared in the crucible, which demonstrates the reliability of the procedure. Figure 3.27 (middle) shows the light yield as a function of τ_2 (hence gas purity) for various TPB thicknesses. The straight lines are fits to a common intersection point. Extrapolation to τ_2 = 3.2 μs lead to the expected light yield for 100% argon purity. The latter is shown as a function of TPB

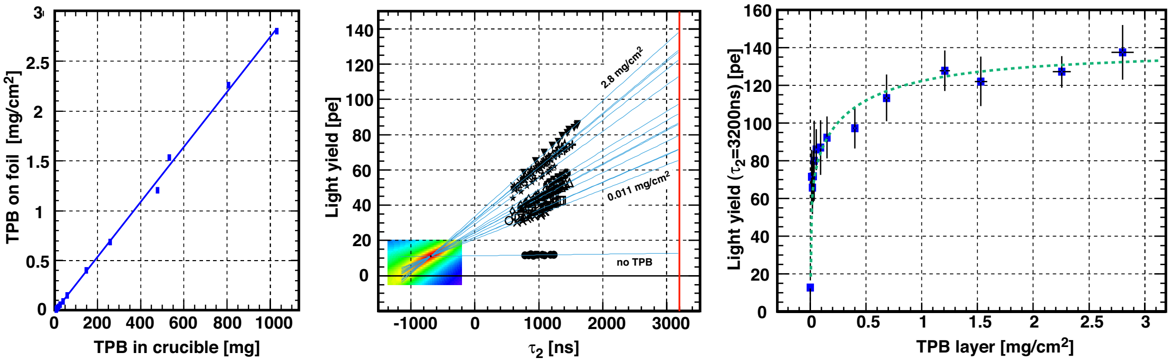

Figure 3.27: *Left: TPB thickness vs. mass in crucible. Middle: number of photoelectrons vs.* τ_2. *Right: number of photoelectrons vs. TPB thickness. The dashed line is drawn to guide the eye.*

thickness in fig. 3.27 (right). Saturation is observed above 1 mg/cm^2 which corresponds to a film of about 10 μm thickness.

A similar correlation between light yield and τ_2 seems to be observed in liquid argon and is the subject of our present investigations. The goal is to collect enough light in liquid to distinguish between nuclear recoils and electrons and to measure the suppression factor for ^{39}Ar background events. In liquid the light output from the α-emitter is quenched by the strong dE/dx and one expects about 15 photons / keV (or 450 photons from a recoiling nucleus of 30 keV), while a minimum ionizing particle leads to 40 photons / keV in the absence of electric field [8].

Our R&D developments for the VUV light yield are encouraging for a large detector volume, the goal being to reach 2%, while 1% has already been achieved. We will therefore proceed with the construction of the one ton prototype in 2007.

References

[1] C. Regenfus, Proc. 6th Int. Workshop on the Identification of Dark Matter (IDM06), Rhode Island, World Scientific, 2006

[2] P. Benetti *et al.* (WARP Collaboration), preprint astro-ph/0603131 (2006)

[3] A. Hitachi *et al.*, Phys. Rev. **B 27** (1983) 5279

[4] G. Eigen, E. Lorenz, Nucl. Instr. Meth. **166** (1979) 165

[5] A. Büchler, Bachelor Thesis, Universität Zürich (2006)

[6] J. Keto *et al.*, Phys. Rev. Lett. **33** (1974) 1365

[7] R. Chandrasekharan *et al.*, Nucl. Instr. Meth. in Phys. Res. **A 546** (2005) 426

[8] P. Cennini *et al.*, Nucl. Instr. Meth. in Phys. Res. **A 432** (1999) 240

4 Publications

Articles

- Study of $K\bar{K}$ resonances in $\bar{p}p \rightarrow K^+K^-\pi^0$ at 900 and 1640 MeV/c
  C. Amsler et al. (CRYSTAL BARREL Collaboration)
  Phys. Lett. **B 639** (2006) 165

- Search for Laser-Induced Formation of Antihydrogen Atoms
  M. Amoretti et al. (ATHENA Collaboration)
  Phys. Rev. Lett. **97** (2006) 213401

- Evidence For The Production Of Slow Antiprotonic Hydrogen In Vacuum
  N. Zurlo et al. (ATHENA Collaboration)
  Phys. Rev. Lett. **97** (2006) 153401

- Progress with cold antihydrogen
  M. Amoretti et al. (ATHENA Collaboration)
  Nucl. Instr. Meth. in Phys. Research **247** (2006) 133

- Review of Particle Physics
  W.-M. Yao et al. (Particle Data Group)
  J. Phys. G : Nucl. and Part. Phys. **33** (2006) 1

- Particle Physics Booklet
  W.-M. Yao et al. (Particle Data Group)
  Institute of Physics Publishing (2006)

- Quark Model
  C. Amsler, T. DeGrand and B. Krusche
  J. Phys. G : Nucl. and Part. Phys. **33** (2006) 165

- The η (1405), η (1475), $f_1(1420)$, and $f_1(1510)$
  C. Amsler and A. Masoni
  J. Phys. G : Nucl. and Part. Phys. **33** (2006) 591

- Non $q\bar{q}$-Mesons
  C. Amsler
  J. Phys. G : Nucl. and Part. Phys. **33** (2006) 949

- The CMS high level trigger
  W. Adam et al. (CMS Collaboration)
  Eur. Phys. J. **C 46** (2006) 605

- A Gaussian sum - Filter for vertex reconstruction
  T. Speer, R. Frühwirth
  Comp. Phys. Comm. **174** (2006) 935

- Track reconstruction in the CMS tracker
  T. Speer et al.
  Nucl. Instr. Meth. in Phys. Research **A 559** (2006) 143

- Robust vertex fitters
  T. Speer et al.
  Nucl. Instr. Meth. in Phys. Research **A 566** (2006) 149

- A double junction model of irradiated silicon pixel sensors for LHC
  V. Chiochia et al.
  Nucl. Instr. Meth. in Phys. Research **A 568** (2006) 51

- Simulation and hit reconstruction of irradiated pixel sensors for the CMS experiment
  E. Alagöz, V. Chiochia, M. Swartz
  Nucl. Instr. Meth. in Phys. Research **A 566** (2006) 40

- Sensor simulation and position calibration for the CMS pixel detector
  V. Chiochia, E. Alagöz, M. Swartz
  Nucl. Instr. Meth. in Phys. Research **A 569** (2006) 132

- Extraction of electric field in heavily irradiated silicon pixel sensors
  A. Dorokhov et al.
  Nucl. Instr. Meth. in Phys. Research **A 560** (2006) 112

- Observation, modeling and temperature dependence of doubly peaked electric fields in irradiated silicon pixel sensors
  M. Swartz et al.
  Nucl. Instr. Meth. in Phys. Research **A 565** (2006) 212

- The control and readout systems of the CMS pixel barrel detector
  D. Kotlinski et al.
  Nucl. Instr. Meth. in Phys. Research **A 565** (2006) 73

- Assembly of the CMS pixel barrel modules
  S. König et al.
  Nucl. Instr. Meth. in Phys. Research **A 565** (2006) 62

- Design and performance of the CMS pixel detector readout chip
  H. Chr. Kästli et al.
  Nucl. Instr. Meth. in Phys. Research **A 565** (2006) 188

- Impact of CMS silicon tracker misalignment on track and vertex reconstruction
  L. Barbone et al.
  Nucl. Instr. Meth. in Phys. Research **A 566** (2006) 45

- CMS Physics technical design report, Volume I : Detector Performance and Software
  CMS Collaboration
  CMS - TDR - 8.1 CERN/LHCC-2006-001
  http://cmsdoc.cern.ch/cms/cpt/tdr/

- CMS Physics technical Design Report, Volume II : Physics Performance
  CMS Collaboration
  CMS-TDR-8.2, CERN/LHCC 2006-021
  http://cmsdoc.cern.ch/cms/cpt/tdr/

- Prospects for B physics at CMS
  T. Speer
  Nucl. Phys. **B (Proc. Suppl.) 163** (2007) 159

- Study of the $B_s \to J/\psi\,\phi\,\mu^+\mu^- K^+K^-$ channel with CMS
  V. Ciulli et al.
  Nucl. Phys. **B (Proc. Suppl.) 156** (2006) 109

- Design and Performance of the Silicon Pixel Detector Modules for the CMS Experiment
  C. Hörmann
  PhD Thesis, Universität Zürich, 2006

Book

- Kern-und Teichenphysik
  C. Amsler
  UTB, Uni-Taschenbücher, Stuttgart, vdf Hochschulverlag AG, ETHZ

Articles in press

- Partial wave analysis of $\bar{p}p$ annihilation at rest into $2\pi^+2\pi^-\eta$
  C. Amsler et al. (Crystal Barrel Collaboration)
  Eur. J. Phys.

- Design and performatnce of silicon sensors for the CMS barrel pixel detector
  Y. Allkofer et al.
  Nucl. Instr. Meth. in Phys. Research **A**

- A new aerogel Čerenkov detector with wavelength shifter
  Y. Allkofer et al.
  Nucl. Instr. Meth. in Phys. Research **A**

- The ATLAS and CMS Detectors and Triggers for B-Physics
  T. Speer
  Nucl. Phys. **B**

- Protonium production in ATHENA at CERN
  L. Venturelli et al.
  Nucl. Instr. Meth. in Phys. Research **B**

- Detection VUV scintillation light in one ton of liquid argon
  C. Regenfus
  World Scientific

Invited Lectures

- C. Amsler
  CHIPP plenary meeting, PSI
  2 October 2006
  "Status of the DIRAC experiment"

- V. Boccone
  Swiss Physical Society, Zürich
  21 February 2006
  "Light readout for the ArDM WIMP-detector"

- V. Chiochia
  8th RD50 Workshop on Radiation Hard Semiconductor Devices for Very High Luminosity Colliders
  25 June 2006
  "Sensor simulation and position calibration for the CMS pixel detector"

- C. Regenfus
  6th Int. Workshop on the Identification of Dark Matter, IDM06, Rhode Island
  13 September 2006
  "Detecting light from WIMPS in 1 ton liquid argon (ArDM)"

- C. Regenfus
  CHIPP Workshop on Neutrino Physics, Bern
  20 October 2006
  "The ArDM experiment"

- T. Speer
  First Workshop on Theory, Phenomenology and Experiments in Heavy Flavour Physics, Capri,
  31 May 2006
  "B-Physics at CMS"

- T. Speer
  7th Int. Conf. on Hyperons, Charm and Beauty Hadrons (BEACH 2006), Lancaster
  7 July 2006
  "The ATLAS and CMS Detectors and Triggers for B Physics"

- L. Wilke
  Swiss Physical Society, Zürich
  21 February 2006
  "Extracting $\Delta\Gamma$ in the B_s-system from angular distributions of the $B_s \rightarrow (J/\psi)\phi$ decay with the CMS detector"

- L. Wilke
  Flavor Workshop in the Era of the LHC
  10 October 2006
  "Study of the Decay $B_s \rightarrow (J/\psi)\phi$ with the CMS Detector"

ATHENA Collaboration (2006):
M. Amoretti, C. Amsler, G. Bonomi, P. Bowe, C. Canali, C. Carraro, C. L. Cesar, M. Charlton, M. Doser, A. Fontana, M. C. Fujiwara, R. Funakoshi, P. Genova, J. S. Hangst, R. S. Hayano, L. V. Joergensen, I. Johnson, A. Kellerbauer, V. Lagomarsino, R. Landua, E. Lodi Rizzini, M. Macri, N. Madsen, G. Manuzio, D. Mitchard, P. Montagna, H. Pruys, C. Regenfus, J. Rochet, A. Rotondi, G. Testera, A. Variola, L. Venturelli, D. P. van der Werf, Y. Yamazaki, N. Zurlo

CRYSTAL BARREL Collaboration (2006):
C. Amsler, C. A. Baker, B. M. Barnett, C. J. Batty, M. Benayoun, P. Blüm, K. Braune, V. Credé, K. M. Crowe, M. Doser, W. Dünnweber, D. Engelhardt, M. A. Faessler, R. P. Haddock, F. H. Heinsius, N. P. Hessey, P. Hidas, D. Jamnik, H. Kalinowsky, P. Kammel, J. Kisiel, E. Klempt, H. Koch, M. Kunze, U. Kurilla, R. Landua, H. Matthäy, C. A. Meyer, F. Meyer-Wildhagen, R. Ouared, K. Peters, B. Pick, M. Ratajczak, C. Regenfus, U. Strohbusch, M. Suffert, U. Thoma, I. Uman, S. Wallis-Plachner, D. Walther, U. Wiedner, B. S. Zou, Č. Zupančič

PARTICLE DATA Group (2006):
W.-M.Yao, C. Amsler, D. Asner, K.S. Babu, R.M. Barnett, J. Beringer, P.R. Burchat, C.D. Carone, C. Caso, O. Dahl, G.D'Ambrosio, A.D. Gouvea, M. Doser, S. Eidelman, J.L. Feng, T. Gherghetta, M. Goodman, C. Grab, D.E. Groom, A. Gurtu, K. Hagiwara, K.G. Hayes, J.J. Hernandez-Rey, K. Hikasa, H. Jawahery, C. Kolda, Y. Kwon, M.L. Mangano, A.V. Manohar, A. Masoni, R. Miquel, K. Mönig, H. Murayama, K. Nakamura, S. Navas, K.A.Olive, L. Pape, C. Patrignani, A. Piepke,

G. Punzi, G. Raffelt, J.G. Smith, M. Tanabashi, J. Terning, N.A. Törnqvist, T.G. Trippe, P. Vogel, T. Watari C.G. Wohl, R.L. Workman, P.A. Zyla

DIRAC Collaboration (2006):
B. Adeva, L. Afanas'ev, Y. Allkofer, C. Amsler, D. Bartos, A. Benelli, V. Brekhovskikh, A. Caragheorgheopol, T. Cechak, M. Chiba, S. Constantinescu, C.O. Curceanu, C. Detraz, D. Dreossi, D. Drijard, A. Dudarev, I. Evangelou, J. L. Fungueirino Pazos, J. Gerndt, P. Gianotti, G. Giolu, O. Gorchakov, K. Gritsay, C. Guaraldo, M. Hansroul, S. Horikawa, M. Iliescu, V. Karpukhin, J. Kluson, M. Kobayashi, P. Kokkas, V. Komarov, L. Kruglova, V. Kruglov, A. Kulikov, A. Kuptsov, K. I. Kuroda, A. Lamberto, A. Lanaro, V. Lapchine, R. Lednicky, P. Levi Sandri, L. Lopez Aguera, V. Lucherini, N. Manthos, C. Marinas Pardo, L. Nemenov, M. Nikitin, K. Okada, V. Ol'shevskiy, M. Pentia, A. Penzo, M. Plo, T.C. Ponta, Z. Pustylnik, G.F. Rappazzo, J. Rochet, A. Romero Vidal, J. J. Saborido Silva, J. Schacher, F. Takeutchi, A. Tarasov, L. Tauscher, F. A. Triantis, T. Trojek, S. Trusov, J. Smolik, S. Sugimoto, A. Ryazantsev, V. Rykalin, O. Vazquez Doce, T. Vrba, V. Yaz'kov, M. Zhabitskiy, P. Zrelov